



UNIVERSIDAD DE SONORA

FACULTAD INTERDISCIPLINARIA DE CIENCIAS
EXACTAS Y NATURALES DEPARTAMENTO DE
INVESTIGACIÓN EN FÍSICA

DESARROLLO Y CALIBRACIÓN DEL SISTEMA
DE MEDICIÓN DE LUMINOSIDAD DEL
DETECTOR DE PÍXELES DE SILICIO CMS

Monografía

En cumplimiento parcial de los requisitos para el grado de:

Doctorado en Ciencias (Física)

By:

Luis Enrique Enrique CUEVAS PICOS

Director:

Dr. Jose Feliciano BENITEZ RUBIO

Hermosillo, Sonora

---, 2025

Acknowledgements

Abstract

Resumen

7 Table of contents

8	List of figures	vii
9	List of tables	viii
10	1 Introduction	1
11	1.1 Particle Physics and The Standard Model	1
12	1.2 Particle Colliders and production cross section	3
13	1.3 Luminosity	6
14	1.4 The Large Hadron Collider	8
15	1.5 Results in Luminosity precision for LHC Run 2	10
16	1.6 Motivation for precise luminosity measurement	11
17	2 Experiment Description	13
18	2.1 The CMS Experiment	13
19	2.2 CMS Luminometers	13
20	2.3 CMS Tracking System	13
21	2.4 Silicon Pixel Detector	13
22	2.5 Pixel Cluster Reconstruction	13
23	3 Luminosity Measurement and Calibration	14
24	3.1 Pixel Cluster Counting method	14
25	3.2 Luminosity calibration: van der Meer method	16
26	3.3 2017 and 2018 data Collected	19
27	3.4 vdM program and Scan types	20
28	3.4.1 2017 vdM scan program	22
29	3.4.2 2018 vdM scan program	23
30	4 Analysis and Results	26
31	4.1 Data acquisition and processing	26
32	4.2 Module selection	26
33	4.2.1 2017 Pixel Detector module selection	28
34	4.2.2 2018 Pixel Detector module selection	29
35	4.3 Background estimation	31
36	4.3.1 Background estimation for 2017 data	31
37	4.3.2 Background estimation for 2018 data	31
38	4.4 Beam Corrections	31

39	4.5	Fit Model Selection	31
40	4.6	Visible cross section results	32
41	4.7	Cross-detector comparisons	32
42	4.8	Systematic Uncertainties	32
43	5	Summary and Outlook	35
44		References	36

45 List of figures

46	1.1	Cross section illustration	5
47	1.2	Colliding beam interaction	6
48	1.3	Luminosity uncertainty in a process	9
49	1.4	LHC Complex	10
50	1.5	Delivered integrated luminosity per year	12
51	3.1	PCC linearity with pile-up	15
52	3.2	Sketch of a vdM scan in x and y directions and example of fitting resulting	
53		rates	19
54	3.3	Cumulative day-by-day integrated luminosity in 2017	20
55	3.4	Cumulative day-by-day integrated luminosity in 2022	20
56	3.5	Doros	23
57	3.6	Doros	25
58	4.1	Profile of good and bad modules stability	27
59	4.2	rms/mean of module weight profile for all modules. A loose selection of	
60		7% is applied to remove bad modules. Appropriate selections are applied	
61		in each iterative step to remove other bad modules.	30
62	4.3	Stability profiles of Pixel detector layers and disks with the final module	
63		selection.	30
64	4.4	Doros	33
65	4.5	Another image caption.	33
66	4.6	Doros	33
67	4.7	Another image caption.	33
68	4.8	Doros	34
69	4.9	Another image caption.	34

70 **List of tables**

71	1.1	The twelve fundamental fermions and their properties	2
72	1.2	Force experienced by the fermions	2
73	1.3	Integrated luminosity values delivered by Run 2	11
74	4.1	PCC 2017 detector module stability selections applied to the module weights	28
75	4.2	Common module vetolist created by combining module vetolists for each	
76		period using a 2% quality selection as described in the text.	29

Chapter 1

Introduction

Particle physics is the branch of physics that studies the fundamental components of matter and the interactions that govern their behavior. It is based on the Standard Model, a theoretical framework that classifies elementary particles into fermions, which make up matter, and bosons, which mediate the fundamental forces (except gravity, which is not yet incorporated into this model). To investigate these particles and their interactions, high-energy particle accelerators are used to generate collisions that allow scientists to measure particle properties and study fundamental phenomena.

This introduction provides a general overview of elementary particles, particle colliders, and the measurement of their properties, establishing the groundwork for studying theoretical and experimental models in particle physics. It highlights key concepts and definitions essential for understanding this project.

1.1 Particle Physics and The Standard Model

Matter and its fundamental interactions are governed by 17 elementary particles that make up the **Standard Model** of particle physics. These particles are divided into two main groups: fermions, which have a spin of $\frac{1}{2}$, and bosons, which have an integer spin. Matter is primarily composed of fermions, which include twelve fundamental particles classified into two types: leptons and quarks. These particles are organized into three generations, with each successive generation having a greater mass than its corresponding particle in the previous generation [1].

The group of six leptons includes three charged particles: the electron (e^-), the muon (μ^-), and the tau (τ^-), along with their corresponding neutrinos: the electron neutrino

(ν_e), the muon neutrino (ν_μ), and the tau neutrino (ν_τ). On the other hand, quarks are only found in hadrons. The group of six quarks consists of: the up quark (u), the down quark (d), the charm quark (c), the strange quark (s), the top quark (t), and the bottom quark (b) [2, 1]. The properties of these twelve particles are summarized in Table 1.1.

Table 1.1 Classification and properties of the twelve fundamental Fermions divided between Quarks and Leptons[1].

Leptons					Quarks			
Generation	Particle		Q	mass/GeV	Particle		Q	mass/GeV
First	electron	(e^-)	-1	0.0005	down	(d)	-1/3	0.003
	e -neutrino	(ν_e)	0	$<10^{-9}$	up	(u)	+2/3	0.005
Second	muon	(μ^-)	-1	0.106	strange	(s)	-1/3	0.1
	μ -neutrino	(ν_μ)	0	$<10^{-9}$	charm	(c)	+2/3	1.3
Third	tau	(τ^-)	-1	1.78	bottom	(b)	-1/3	4.5
	τ -neutrino	(ν_τ)	0	$<10^{-9}$	top	(t)	+2/3	174

Bosons act as mediators of interactions between fermions by exchanging particles known as gauge bosons. The electromagnetic force is mediated by the photon (γ), which interacts with charged particles such as electrons (e^-) and protons (p). The weak force is mediated by the W^\pm and Z^0 bosons, interacting with all leptons and quarks, facilitating processes like beta decay in nuclei. The strong force, responsible for holding quarks together within protons and neutrons, is carried by gluons (g), and it only interacts with quarks and gluons themselves, forming the strong interaction that binds hadrons together. Additionally, the Higgs boson, a scalar boson, plays a crucial role in providing mass to all fundamental particles through the Higgs mechanism, which affects both fermions and bosons [1]. Table 1.2 provides a comprehensive overview of the forces experienced by fermions.

Table 1.2 Force experienced by the fermions [1].

				Electromagnetic	Weak	Strong
Leptons	e^-	μ^-	τ^-	✓	✓	
	ν_e	ν_μ	ν_τ		✓	
Quarks	u	c	t	✓	✓	✓
	d	s	b	✓	✓	✓

So far, the Standard Model (SM) of particle physics is the most precise and successful theoretical model for describing experimental data available to date. This model provides a detailed explanation of the fundamental interactions between elementary particles. However, most of this data comes from experiments conducted at particle colliders, as these

120 devices allow the production and study of particles through high-energy collisions, making
121 it possible to observe phenomena that cannot be studied otherwise. Despite its success, the
122 Standard Model still has limitations and cannot explain some aspects of the universe, such
123 as gravity, dark matter, and dark energy.

124 **1.2 Particle Colliders and production cross section**

125 Particle colliders are powerful scientific instruments used to produce, accelerate, and collide
126 beams of particles at relativistic speeds, enabling scientists to explore the fundamental
127 properties of matter and the universe. These experiments function as powerful microscopes
128 that allow researchers to study subatomic particles such as electrons, protons, neutrons,
129 neutrinos, and quarks. They also provide a means to test predictions made by the Standard
130 Model.

131 The high speeds required for the collisions are achieved through the use of powerful
132 superconducting magnets, which accelerate particles to the necessary velocities. These
133 particles are then collided at specific points along the accelerator, where detectors are
134 located. These detectors are capable of measuring individual interactions, known as events,
135 generated by the collisions. Some of the particles produced, such as the Higgs boson,
136 cannot be directly observed. Instead, they are detected and analyzed using advanced
137 technologies, which measure their interactions with matter [1].

138
139 In general, a particle detector is typically constructed as a cylindrical or polygonal
140 barrel section, oriented parallel to the incoming colliding beams. Two flat end caps seal
141 the cylindrical structure, ensuring nearly complete solid angle coverage all the way down
142 to the beam pipe. This detector comprises multiple layers, each designed to detect the
143 different particles generated during collisions [1].

144
145 Particle colliders are evaluated based on two important measures, which are the avail-
146 able center of mass energy and the rate at which particles collide (luminosity). The amount
147 of energy that is available to create new particles and study their properties is particularly
148 significant because it determines the range of particles that can be produced. During exper-
149 iments, particles are accelerated and directed toward each other, and when they collide,
150 they produce new particles and interactions that can be analyzed by scientists.

151
152 Colliding beam machines are capable of achieving significantly higher energies at the
153 point where the beams intersect and scatter. When the particles in the beams have equal

energy and opposite momentum (equal mass), the experiment occurs in the center-of-mass (CM) frame. This allows for the entire energy delivered by the accelerator to be utilized in generating high-mass particles [3]. In particle physics, the Lorentz invariant quantity s represents the square of the total incoming energy and is defined as:

$$s = \left(\sum_{i=1,2} E_i \right)^2 - \left(\sum_{i=1,2} p_i \right)^2 c^2 \quad (1.1)$$

Where p and E are the momenta and the energy of each incoming particle respectively. In the center-of-mass (CM) frame, where the momenta of the particles are equal and opposite, the second term in the equation for the Lorentz invariant quantity (s) disappears, leaving only $s = 4E^2$.

The second important parameter used to evaluate the performance of colliders is luminosity, which measures the accelerator's ability to produce the necessary number of interactions. It is determined by the proportionality factor between the quantum mechanical probability for the interaction (known as the cross section) and the number of events for a specific physics process per second (R) [4].

The technical meaning of "cross section" in particle physics is quite different from its common usage, while "cross section" typically refers to a slice of an object, in particle physics, it quantifies the probability of a collision and is a property of the interaction of one particle with another, this is expressed in units of square meters. When two beams cross in a particle accelerator, a variety of different processes can occur and the cross section of a given process depends on the type and energy of the colliding particles. At the Large Hadron Collider (LHC), certain particles such as W^\pm and Z^0 bosons have large cross sections, making their observation more frequent, while the production of a Higgs boson has a much lower cross section, making it more difficult to produce [1].

To explain this concept more clearly, let's consider a simple scenario where a beam of particles of type a passes through a region of space that contains particles of type b . The interaction rate between the two types of particles depends on the number of particles per unit volume of type b , denoted as n_b , and the flux of the incident particles, denoted as ϕ_a . The rate of interaction per target particle of type b can be expressed as follows:

$$r_b = \sigma \phi_a$$

184 The essence of fundamental physics can be encapsulated in the interaction cross
 185 section, denoted by σ . This parameter, which is measured in area units, represents the
 186 likelihood that an interaction will occur between an incident particle and a target particle.
 187 It's helpful to imagine each target particle as having an effective cross-sectional area, and
 188 the interaction cross section as representing that area. Figure 1.1(a) shows an illustration of
 189 this concept, where an incident particle of type a moves with velocity v_a through a region
 190 of area A that contains target particles of type b with velocity v_b moving in the opposite
 191 direction. The value of the interaction cross section is determined by the underlying
 192 quantum mechanical probability of interaction and is fundamental to understanding the
 193 behavior of particles in collisions. [1]

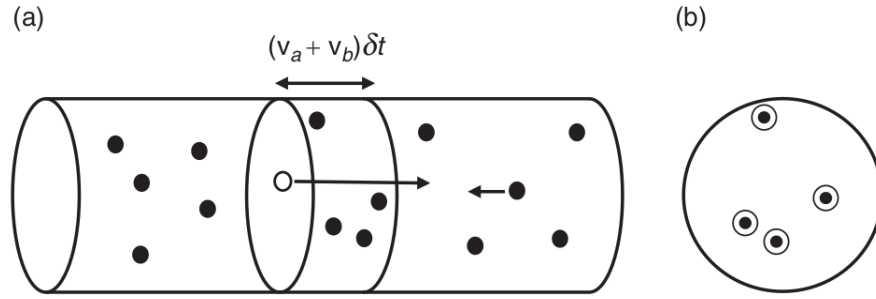


Fig. 1.1 Left hand (a): single incident particle of type a traversing a region containing particles of type b . Right-hand plot (b): projected view of the region traversed by the incident particle in time δt .

194

195 To understand the probability of an interaction between particles of types a and b ,
 196 imagine that in a time interval δt , particle a passes through a region containing $\delta N =$
 197 $nb(v_a + v_b)A\delta t$ particles of type b . The probability of interaction can be obtained by
 198 dividing the effective total cross-sectional area of the δN particles by the area A . This can
 199 be thought of as the probability that the incident particle passes through one of the regions
 200 of area σ drawn around each of the δN target particles, as shown in Figure 1.1(b). So the
 201 cross section for a particular process is defined as the effective target area for that process
 202 and has units of area, more formally is expressed as 1.2 [1].

$$\sigma = \frac{\text{number of interaction per unit time per target particle}}{\text{incident flux}} \quad (1.2)$$

1.3 Luminosity

In experiments conducted in particle physics, the number of useful interactions (or events) is just as important as the energy. The ability of a particle accelerator to produce these interactions is measured by a parameter called instantaneous luminosity \mathcal{L}_{inst} . It is directly proportional to the number of events produced per second and the cross section σ_p [5].

$$R = \mathcal{L}_{inst} \cdot \sigma_p \quad (1.3)$$

Where the unit of luminosity is $cm^{-2}s^{-1}$.

To derive a general expression for luminosity in the case of two colliding beams, we consider both beams to serve as the target and the incoming beam simultaneously. We will assume that the beams are "bunched", meaning that the particles are grouped into packets or bunches.

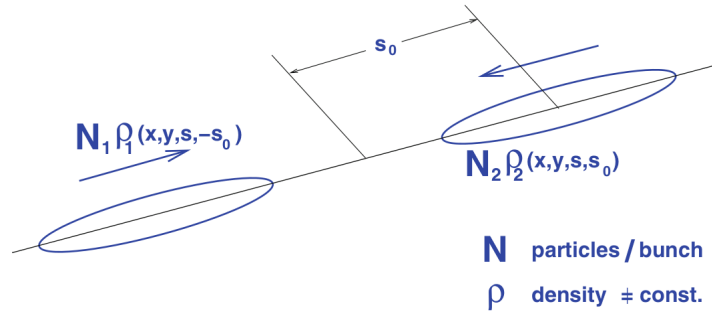


Fig. 1.2 Schematic view of a colliding beam interaction[5]

In Figure 1.2, you can see a diagram that illustrates how two beams intersect with each other. Because these beams are not still, but rather in motion, the way they overlap depends on the time and the position of the bunches. While the beams move, they also have different distributions and numbers of particles in them [5]. The luminosity \mathcal{L}_{inst} , which is proportional to the overlap integral, can be expressed as:

$$\mathcal{L}_{inst} \propto K \cdot \int \int \int \int_{-\infty}^{\infty} \rho_1(x, y, s, -s_0) \rho_2(x, y, s, s_0) dx dy ds ds_0 \quad (1.4)$$

The functions $\rho_1(x, y, s, -s_0)$ and $\rho_2(x, y, s, s_0)$ represent the beam density distribution at a given time. We assume that the two bunches meet at the point $s_0 = 0$. Since the beams are in motion towards each other, we need to take into account a relativistic kinematic factor (Eq. 1.5) by multiplying this expression.

$$K = \sqrt{(\vec{v}_1 - \vec{v}_2)^2 - (\vec{v}_1 \times \vec{v}_2)^2/c^2} \quad (1.5)$$

When the bunches collide head-on and are traveling at nearly the speed of light, the relativistic kinematic factor takes on a value of 2. Assuming uncorrelated densities in all planes and head-on collisions where the velocities of the two bunches are opposite ($\vec{v}_1 = -\vec{v}_2$), the overlap integral can be factorized as:

$$\mathcal{L}_{inst} = 2N_b N_1 N_2 f \int \int \int \int_{-\infty}^{\infty} \rho_{1x}(x) \rho_{1y}(y) \rho_{1s}(s - s_0) \rho_{2x}(x) \rho_{2y}(y) \rho_{2s}(s + s_0) dx dy ds ds_0 \quad (1.6)$$

where N_b is the number of bunches in one beam, N_1 and N_2 are the particles per bunch and f the revolution frequency.

Assuming Gaussian profiles in all dimensions and approximately equal bunch lengths ($\sigma_{1s} \approx \sigma_{2s}$), the equation 1.6 can be solved. For a general case where $\sigma_{1x} \neq \sigma_{2x}$ and $\sigma_{1y} \neq \sigma_{2y}$

$$\mathcal{L}_{inst} = \frac{N_1 N_2 N_b f}{2\pi \sqrt{\sigma_{1x}^2 + \sigma_{2x}^2} \sqrt{\sigma_{1y}^2 + \sigma_{2y}^2}} \quad (1.7)$$

For a specific case, assuming equal beams, $\sigma_{1x} = \sigma_{2x}$ and $\sigma_{1y} = \sigma_{2y}$:

$$\mathcal{L}_{inst} = \frac{N_1 N_2 N_b f}{4\pi \sigma_x \sigma_y} \quad (1.8)$$

This expression is widely recognized as the formula for the luminosity of two Gaussian beams that collide head-on. It reveals how the luminosity is related to the number of particles in each bunch and the size of the beams [5].

In practice, the integral in 1.6 cannot be solved analytically because the properties of the colliding beams are not known precisely, so an experimental technique is implemented with a dedicated machine setup to estimate the integrals, yielding a similar expression as 1.8.

To determine the overall number of events, we rely on integrated luminosity, which is a measurement of the total amount of collected data. This value is crucial for evaluating the effectiveness of an accelerator and it can be expressed as: [5]:

$$\mathcal{L}_{int} = \int_0^T \mathcal{L}_{inst}(t') dt' \quad (1.9)$$

Where the value of \mathcal{L}_{inst} is evaluated over time T (excluding possible dead time) because its intensity decreases as the number of protons reduces during the collisions of the fill. So \mathcal{L}_{int} is directly related to the number of observed events as:

$$\mathcal{L}_{int} \sigma_p = \text{number of events of interest} \quad (1.10)$$

The integrated luminosity has units of cm^{-2} and is often expressed in inverse barn ($1barn = 10^{-24}cm^2$).

Precisely understanding luminosity is really important for physics analyses like finding new particles, measuring known particle properties, or detecting rare processes. The accuracy of our physics measurements is mainly affected by uncertainties in luminosity. If we can increase the precision of luminosity measurements, then physicists will have a better understanding of their observations and be able to explore parts of physics that we don't currently know about [6].

An example of this can be seen in Fig. 1.3, which illustrates the production of W and Z bosons in the large hadron collider. In this figure, the inner error bars represent the experimental uncertainties, while the outer error bars encompass the uncertainties in the theoretical predictions. Additionally, the shaded box indicates the uncertainties in the luminosity measurement, which is bigger than statistical and other systematics uncertainties [7].

1.4 The Large Hadron Collider

The Large Hadron Collider (LHC) is the world's biggest and most potent particle accelerator. It became operational on 10th September 2008 and is the most recent addition to CERN's accelerator complex. The LHC consists of a 27-kilometer ring that contains superconducting magnets, and various structures are used to accelerate particles as they move along the ring. Inside the accelerator, two particle beams travel at almost the speed of light until they collide. The beams move in opposite directions in separate beam pipes, which are kept at an ultra-high vacuum.

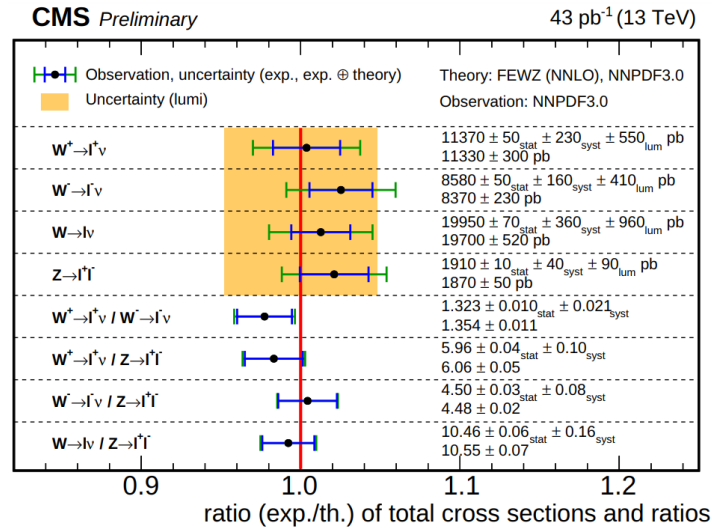


Fig. 1.3 Production of W^+ , W^- , W and Z bosons and their theoretical predictions. The shaded box indicates the uncertainties in the luminosity measurement, showing that is bigger than the experimental (blue bars) and theoretical (green bars) uncertainties. The measurements and theoretical predictions values are on the right

Superconducting electromagnets generate a powerful magnetic field that guides the particle beams around the accelerator ring. These magnets are made up of coils of a unique electric cable that functions in a superconducting state. In this state, the cable can conduct electricity with zero resistance or energy loss. The accelerator uses a variety of magnets, including 1232 dipole magnets that are 15 metres in length and bend the beams, and 392 quadrupole magnets that are 5-7 metres long and focus the beams. Just before the collision, a different type of magnet is employed to "squeeze" the particles together, increasing the likelihood of collisions. To keep these magnets in the superconducting state, they must be cooled to a temperature as low as -271.3°C [8].

The process of generating proton beams for the LHC is a complex and multi-stage procedure. Initially, hydrogen is ionized to create protons, which are then accelerated in bunches up to 50 MeV in the Linear Accelerator 2 (LINAC2). The proton bunches are then routed through three circular accelerators: the Booster, the Proton Synchrotron (PS), and the Super Proton Synchrotron (SPS). These accelerators gradually increase the energy levels of the proton bunches to 1.4 GeV, 26 GeV, and 450 GeV, respectively [9]. Once these pre-acceleration stages are completed, the proton bunches are injected into the LHC ring where they are further accelerated to achieve energies of up to 7 TeV per bunch while circulating in opposite directions. This entire process constitutes a single LHC fill and typically involves 10^{14} protons that are grouped into bunches to form the proton beam. The complete CERN accelerator complex is illustrated in Figure 1.4.

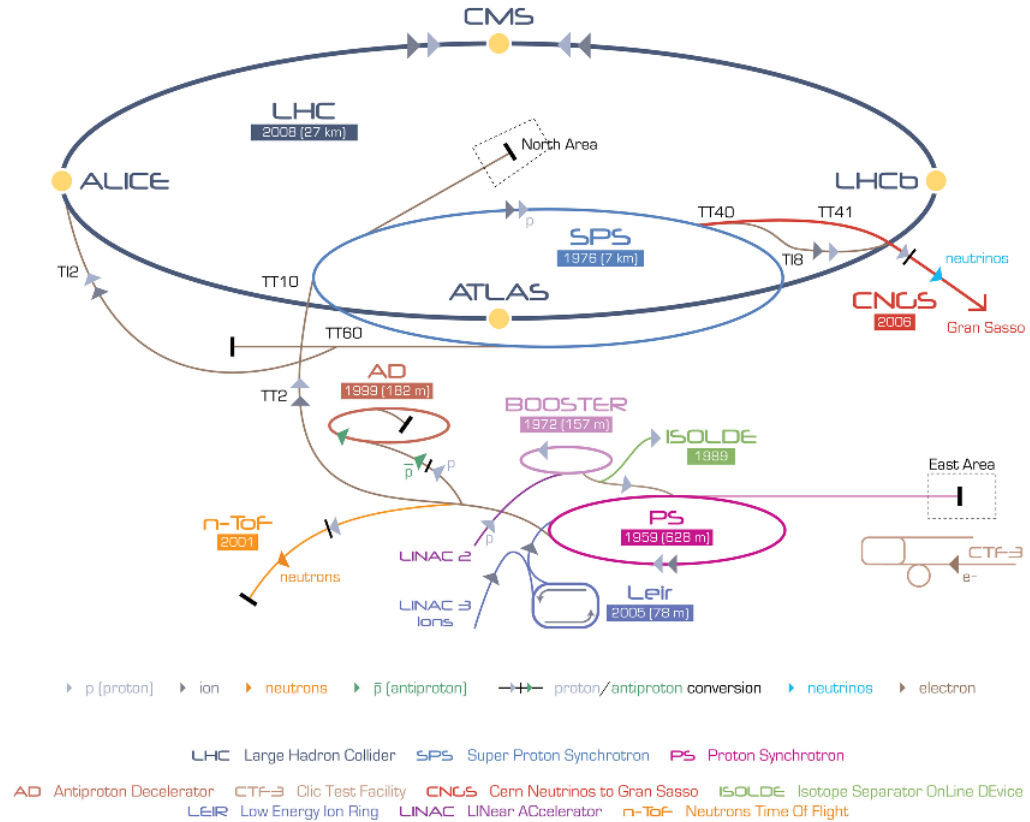


Fig. 1.4 Diagram of the LCH complex [9].

294

295 The CERN Control Centre serves as the central hub responsible for managing all
 296 controls, services, and technical infrastructure of the LHC. It directs the proton beams to
 297 collide at four distinct locations along the accelerator ring, corresponding to the positions
 298 of four particle detectors: CMS and ATLAS, which are general-purpose detectors designed
 299 to explore a broad range of Standard Model (SM) and Beyond SM (BSM) physics, while
 300 ALICE and LHCb are specialized detectors that focus on studying specific phenomena.

301 1.5 Results in Luminosity precision for LHC Run 2

302 Since its inception in 2010 the LHC has undergone three runs and two lengthy shutdowns
 303 for maintenance and upgrades. Run1 began in 2010 with proton-proton collisions at a
 304 center-of-mass energy of $\sqrt{s} = 7$ TeV and concluded in 2012 at $\sqrt{s} = 8$ TeV. Run 2, which
 305 took place at $\sqrt{s} = 13$ TeV, was divided into two stages; the first occurred from 2015 to
 306 2016.

307

308 The second stage (2017–2018) had preliminary results published in the Public Analysis
 309 Summaries, CMS-PAS-LUM-17-001 [10] for 2018 and CMS-PAS-LUM-18-002 [11] for
 310 2017. However, the desired uncertainty values were not achieved. Efforts are currently
 311 underway to further improve the precision of these measurements and present them in a
 312 final publication. This project is primarily focused on contributing to this publication by
 313 analyzing the PCC luminometer and refining the uncertainty, aiming to achieve values of
 314 approximately 1%.

315
 316 The integrated luminosity for Run 2, along with its corresponding uncertainty values,
 317 is presented in Table 1.3. These luminosity values account for the period from the start of
 318 stable beams until the beam is dumped by the LHC. Additionally, Figure 1.5 provides a
 319 visualization of the delivered luminosity over time for each year, as measured by CMS.

Table 1.3 Integrated luminosity values delivered by Run 2 (precision values for the years 2017 and 2018 show preliminary results)

Period	Energy \sqrt{s}	Integrated Luminosity	Precision
Run 1(2010-2012) [12]	8 TeV	$30 fb^{-1}$	2.2%
Run 2(2015-2016) [13]	13 TeV	$45.9 fb^{-1}$	1.6%-1.2%
Run 2(2017) [10]	13 TeV	$49.8 fb^{-1}$	2.3%
Run 2(2018) [11]	13 TeV	$67.9 fb^{-1}$	2.5%

320

321 1.6 Motivation for precise luminosity measurement

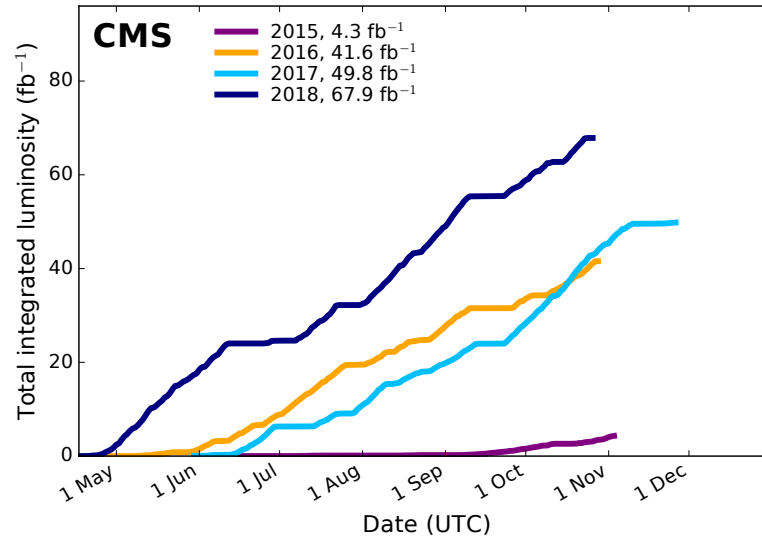


Fig. 1.5 Delivered luminosity versus time for Run-1 (2010-2012) and Run-2 (2015-2018) and Run-3 that is still ongoing . Cumulative luminosity versus day delivered to CMS during stable beams for pp collisions at nominal center-of-mass energy. [14].

322 **Chapter 2**

323 **Experiment Description**

324 **2.1 The CMS Experiment**

325 **2.2 CMS Luminometers**

326 **2.3 CMS Tracking System**

327 **2.4 Silicon Pixel Detector**

328 **2.5 Pixel Cluster Reconstruction**

Chapter 3

Luminosity Measurement and Calibration

Accurate measurement of the luminosity delivered to the CMS experiment by the LHC is essential for various reasons. Online, the luminosity measurement provides feedback on the LHC and CMS performance and operations, including measuring trigger rates. In offline analysis, the luminosity measurement is a critical component for measuring the cross-section of observed processes or setting upper limits in searches for processes beyond the standard model.

As we see, to measure luminosity, a total of seven luminometers are used at CMS, and each of them reads out a specific quantity observed in the detector, such as hits, tracks, or clusters. The rate R measured by the luminometer is proportional to the instantaneous luminosity, \mathcal{L}_{inst} , with the constant of proportionality given by the visible cross-section σ_{vis} [11].

$$R(t) = \mathcal{L}_{inst} \sigma_{vis} \quad (3.1)$$

The determination of σ_{vis} is performed through van der Meer (vdM) scans using a specialized LHC machine setup. This chapter provides a description of this procedure, specifically applied with the PCC method.

3.1 Pixel Cluster Counting method

The PCC method is an offline technique that provides a luminosity measurement using the rate of pixel clusters. Due to the large area of the pixel detector and the relatively low occupancy of its sensors, the probability of a single pixel being struck by two charged

particles from the same bunch crossing is extremely low. This high granularity and low occupancy result in an excellent linear response to pile-up (μ , the number of interactions per bunch crossing) [12]. On average, the detector occupancy (hit pixels/ total pixels) is less than 0.1% [13]. Although the statistical precision per Lumisection (23-second period) is lower than that of online luminometers due to CMS trigger bandwidth limitations, PCC still provides a linear measurement with good precision over time. When integrated over longer periods, it delivers a stable and highly precise luminosity measurement.

Figure 3.1 shows a simulation with pp collision zero-bias events with the pixel cluster counting rate as a function of pileup in the pileup range observed in Run 2 from 0 to about 50 μ . Where the mean number of pixel clusters is of the order of 111 per event. The red curve is a first-order polynomial fit with slope, the results indicate a high level of agreement, as evidenced by the estimated goodness-of-fit χ^2 per degree of freedom (dof) of approximately 0.5, showing that the PCC rate is highly linear in this range under simulated conditions [15, 13].

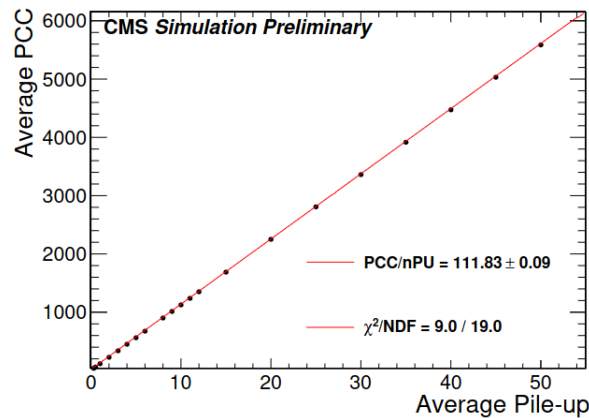


Fig. 3.1 Linearity of pixel cluster counting over the pileup range observed in Run 2 (from 0 to about 50) from simulation. The red line is a linear fit to the points [15]

For physics conditions, two data streams are recorded via the CMS DAQ: "zero-bias" and "random." The zero-bias stream consists of triggered data for colliding bunches at a bandwidth of approximately 2 kHz, while the random stream collects triggered data from all bunch crossings at a bandwidth of 500 Hz, primarily used for background estimation. The luminosity measurement is performed using the zero-bias data, whereas the random trigger helps evaluate background contributions.

Under vdM conditions, a special trigger mode is employed to achieve higher data rates for PCC. This mode focuses on a selected set of five colliding bunch crossings, as detailed for each year in the next chapter, ensuring the necessary statistical precision.

374 To derive the luminosity measurement from the PCC method, the mean number of
 375 pixel clusters per event is computed by averaging over several zero-bias events. This value
 376 is given by:

$$\langle N_{\text{cluster}} \rangle \equiv \langle N_{\text{cluster/interaction}} \rangle \mu \quad (3.2)$$

377 Under minimum bias conditions, μ can be expressed as:

$$\mu = \frac{\sigma_{\text{minBias}}}{f} \cdot \mathcal{L}_{\text{inst}} \quad (3.3)$$

378 where f is the LHC revolution frequency and $\mathcal{L}_{\text{inst}}$ is the single bunch instantaneous
 379 luminosity (SBIL). The minimum bias cross section σ_{minBias} here is related to the PCC
 380 visible cross section by the mean number of clusters per interaction:

$$\sigma_{\text{vis}} = \langle N_{\text{cluster/interaction}} \rangle \cdot \sigma_{\text{minBias}} \quad (3.4)$$

381 Combining everything, the PCC luminosity measurement is obtained as:

$$\mathcal{L}_{\text{inst}} = \frac{\langle N_{\text{cluster}} \rangle f}{\sigma_{\text{vis}}} \quad (3.5)$$

382 In the PCC measurement, the innermost layer (Layer 0) of the pixel detector is excluded
 383 due to significant dynamic inefficiency effects. At high instantaneous luminosities, the hit
 384 efficiency decreases because the readout chip cannot process all hits in time.

385 For PCC rate measurements, only the pixel detector modules that remain stable through-
 386 out the entire data-taking period (year) are used. Modules known to be defective or
 387 significantly affected by the limited size of the readout buffer are excluded from the
 388 analysis.

389 The final number of excluded modules, referred to as "veto modules," is detailed for
 390 each year in the next chapter.

391 **3.2 Luminosity calibration: van der Meer method**

392 As discussed in Chapter 1, the instantaneous luminosity for a single colliding bunch is
 393 described by Eq. (1.6). In practice, while the measurement of the beam currents $N_{1,2}$
 394 is well determined, the individual proton density functions cannot be directly measured.
 395 To address this, the vdM method involves a specific machine setup that allows for the

determination of the two beam overlap integrals. This is achieved by varying the separation between the beams and measuring the resulting rates, which can be used to obtain density profiles that are close to normal distributions. The beam overlap can be expressed in terms of the measured rates as follows:

$$\int \rho_{x1}(x)\rho_{x2}(x)dx = \frac{R_x(0)}{\int R_x(\Delta)d\Delta} \quad (3.6)$$

where $R_x(\Delta)$ is the rate measured when the two beams are separated in x by a distance Δ ; a similar equation can be written in y . Then the beam overlap width Σ_x (and similarly Σ_y) is defined as [11]:

$$\Sigma_x = \frac{1}{\sqrt{2\pi}} \frac{\int R_x(\Delta)d\Delta}{R_x(0)} \quad (3.7)$$

This process leads to the final expression for luminosity for a single colliding bunch:

$$\mathcal{L}_{inst} = \frac{N_1 N_2 f}{2\pi \Sigma_x \Sigma_y} \quad (3.8)$$

where $N_{1,2}$ are the particles per bunch (bunch current) and $f = 11246$ Hz is the bunch orbit frequency around the LHC ring determined by the energy of the protons.

Therefore, the equation 3.1 used to measure the visible cross sections σ_{vis} takes the following form:

$$\sigma_{vis} = 2\pi \frac{R(0,0)}{N_1 N_2 f} \Sigma_x \Sigma_y \quad (3.9)$$

Experimentally, the quantities Σ_x and Σ_y , as defined in Eq. (3.7), are determined by conducting two separate scans in the x and y directions, respectively. These scans are performed by varying the separation between the beams in each direction at a fixed number of separation steps. The separation steps are determined through curve fitting of the scan data based on the luminometer rate measurements obtained during the vdM scans.

The measured rate, denoted by $R(0,0)$, is determined as the average value among the rates obtained in the x -scan $R_x(0)$, and the rates obtained in the y -scan $R_y(0)$. Although the beam widths are identical for all luminometers, the peaks of the scan curves are specific for each luminometer.

420 Figure 3.2 depicts a schematic of the beam positions during vdM scans in the x and y
421 planes, along with the detector rate as a function of beam separation [11].

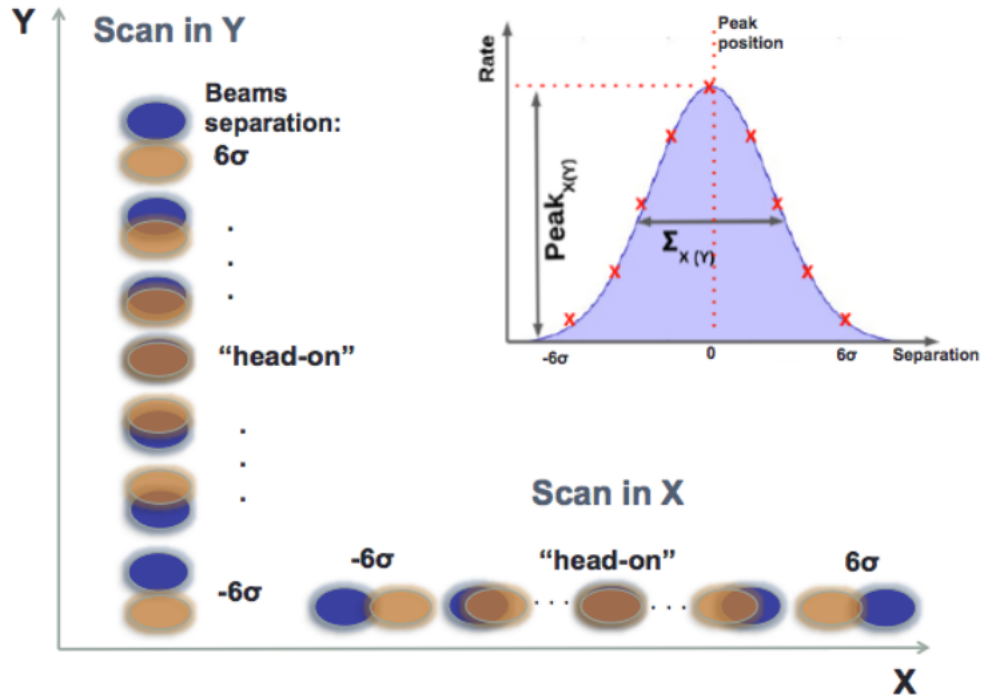


Fig. 3.2 The sketch of a vdM scan in x and y planes. The indent sketch is an example of the fit of the resulting rates [16].

3.3 2017 and 2018 data Collected

In June 2017, data collection for the second phase of Run 2 of the Large Hadron Collider (LHC) began, covering the years 2017 and 2018. As a result, a total recorded luminosity of 49.81 fb^{-1} for 2017 and 67.86 fb^{-1} for 2018 was achieved. This data was collected during proton-proton collisions at a center-of-mass energy of $\sqrt{s} = 13 \text{ TeV}$.

The data-taking period started with the establishment of stable beams and ended either when the beam was intentionally stopped or when stable beams were temporarily interrupted for beam studies.

Each year, a dedicated setup is allocated for the van der Meer (vdM) program, which will be discussed in a later chapter. This program is essential for the calibration of luminosity and the determination of its associated uncertainty, which plays a crucial role in the analyses where luminosity is a key factor.

The luminosity delivered by the LHC to CMS (shown in blue) and the luminosity recorded by CMS (depicted in orange) during 2017 are illustrated in Figure 3.3, while Figure 3.4 presents the corresponding data for 2018 [14].

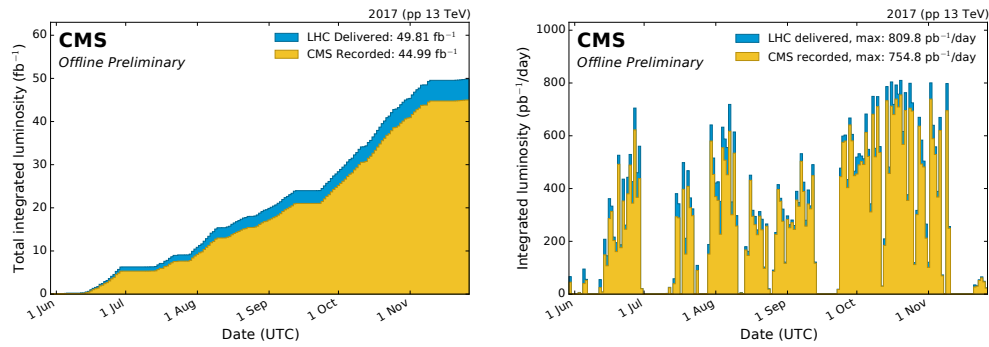


Fig. 3.3 (left) Cumulative day by day integrated luminosity. (right) Day by day integrated luminosity, 2017 as the first plot, but not cumulative.

438

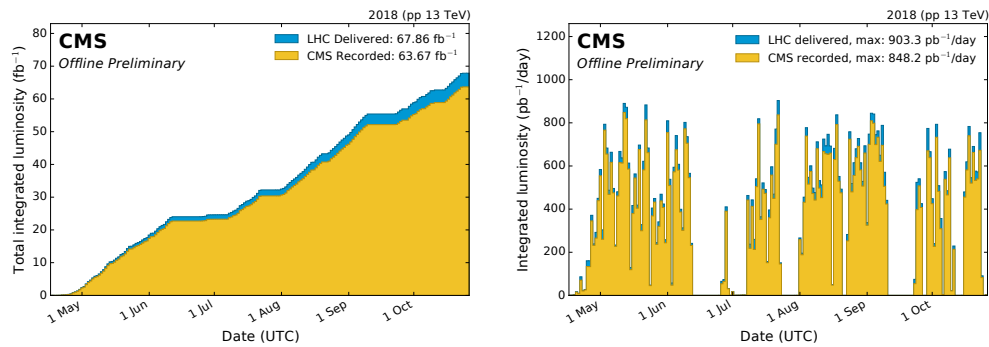


Fig. 3.4 (left) Cumulative day by day integrated luminosity. (right) Day by day integrated luminosity, 2018 as the first plot, but not cumulative.

439

3.4 vdM program and Scan types

440

Each year, the vdM scan program for the CMS experiment is conducted during specific LHC fills using a dedicated setup. The LHC filling schemes are designed with a specific number of bunch pairs at the CMS interaction point (IP5), for the specific case of 2017 an 2018 was at a proton-proton collision energy of $\sqrt{s} = 13$ TeV. These scans play a crucial role in the precise determination of the luminosity by measuring the transverse beam profiles and overlap integral.

To minimize long-range beam-beam effects and detector afterglow, the bunches are arranged in a way that optimizes the measurement conditions. During these special fills,

447

448

the beams are systematically displaced in the transverse plane, allowing for a detailed study of beam dynamics and interaction rates. Various types of scan pairs with different characteristics were conducted to refine the accuracy of the luminosity determination.

Each scan pair consisted of two scans in the transverse x and y planes. These included standard vdM scans, emittance scans, beam imaging scans, offset scans, and length scale calibration scans, each serving a specific purpose in the measurement process. A detailed description of each scan is provided below.

Standard vdM: used specifically to compute σ_{vis} , in this scan the two beams are separated by $6\sigma_b \approx 578\mu m$, where σ_b represents the transverse bunch size. and scanned across each other in a sequence of 25 steps with 30 seconds per step with a step size of $0.5\sigma_b \approx 48\mu m$ in either the horizontal (x) or vertical (y) direction.

Emittance: same procedure as the standard vdM scans except the maximum separation (2.5 $4b$), the number of steps (7 or 9) and the time per step (10 seconds) are smaller, so that the scan takes a shorter time. These type of scans are also performed in physics conditions as discussed in Section.

Beam imaging: in these scans, one beam (beam 1 and beam 2, respectively) is kept fixed at its nominal head-on position, while the other beam is separated and scanned in 19 steps, each step lasts 46 seconds and covers a range from $-4.5\sigma_b$ to $+4.5\sigma_b \approx 433\mu m$. These scans were developed for studies on beam shapes, estimating the uncertainty caused by the correction called x - y non-factorization described in the next chapter. BI scans are also analyzed as traditional vdM scans and used to compute of σ_{vis} .

Constant-Separation Length Scale: during this scan the two beams are separated by $\sqrt{2}\sigma_b \approx 106\mu m$ (approximately equal to $1\sigma_b$) and moved together in steps of $1\sigma_b$ forward and backward in five steps each, for a total of 10 steps with 70 seconds per step.

Variable-Separation length scale: one beam (starting with beam 1) is moved to $-2.5\sigma_b$ and then a three-point scan is performed with the other beam (starting with beam 2) at arelative position of $+ - 1.25\sigma_b$, 0, and $+1.25\sigma_b$. The position of the first beam is then stepped in five steps to $+2.5\sigma_b$, repeating the three-point scan (“miniscan”) at each step. This procedure is repeated four times, with two directions for each of the two beams. Each scan point has a duration of about 46 s.

The two types of Length scale are pecial scan designed to apply a correction to the results of σ_{vis} obtained from the vdM scan program, this correction will be described

485 further in this section.

486

487 **Offset:** same procedure as the standard vdM scans except that the beams are separated by
488 range from $-3\sigma_b$ to $+3\sigma_b$ in the non-scanning direction.

489

490 **Super Separation:** this type of scan is performed for background estimation. In this scan,
491 the two beams are separated by a distance of $6\sigma_b$ for 5 minutes. At this distance, the
492 beam overlap is minimal, and the contribution from collisions is negligible. There can be
493 more than one Super Separation scan per scan program, this is useful to understanding the
494 behavior of the background throughout the year and for subtracting it accordingly.

495 The data collected from these scans provide the essential input for luminosity calibra-
496 tion, which is critical for cross-section measurements and precision physics analyses at the
497 LHC.

498 3.4.1 2017 vdM scan program

499 The 2017 vdM scan program was performed during LHC fill 6016 on 28 July 2017, at a
500 center-of-mass energy of 13 TeV. The LHC filling scheme included 32 colliding bunch
501 pairs at the CMS interaction point (IP5). In the special case of PCC, to ensure a dataset
502 with a high event count at large beam separations, CMS gated the zero-bias triggers on 5
503 bunch pairs (BCIDs 41, 281, 872, 1783, and 2063) and recorded events at a total rate of 18
504 kHz.

505 The bunch intensities were approximately 9×10^{10} protons per filled bunch, resulting
506 in a total beam intensity of approximately 4.5×10^{12} protons per beam. The total beam
507 intensities were measured with the DC Current Transformers (DCCT) [17]. The beam
508 orbit was monitored using two systems: the DOROS beam position monitors (BPMs) [18],
509 located near IP5, and the arc BPMs, located in the LHC arcs adjacent to CMS.

510 The vdM scan program consisted of a total of eight orthogonal (x-y) scan pairs. It
511 started with a short emittance scan, em1. Four scans were standard vdM scans: vdM1 (2),
512 vdM3 (6), and vdM4 (11). These scans were performed first in the x direction and then in
513 the y direction. The intermediate scan, vdM2 (3), was performed first in the y direction
514 and then in the x direction. This was done to check reproducibility.

515 Two scan pairs of beam imaging scans were performed, with beam 1 and beam 2
516 scanning. Pairs Im1 and Im2 corresponded to scans 4 and 5, respectively. Scan pair 7 was
517 an offset scan (off) performed just after vdM3, but it is not used in this analysis.

518 A length scale calibration (LSC) program was performed at the end of the vdM program
 519 using two different LS methods. The first method was the constant-separation scan (cLS),
 520 performed as scan 8 in this program. This type of scan had been previously used in the
 521 2015–2016 publication [13] for the CMS length scale calibration.

522 The second method consisted of variable-separation scans, vLS1 and vLS2, which
 523 were scans 9 and 10, respectively, in the LS program. This method was used for the first
 524 time in 2017, following the scan protocol originally developed by ATLAS.

525 The top of Figure 4.8 shows the beam positions for the two beams in the x and y
 526 directions as measured by the DOROS BPMs during the 2017 scan program, showing the
 527 four regular scan pairs, the two beam imaging scan pairs, the offset scan pair, and the two
 528 length scale scan programs, with the abbreviations used for the scans introduced.

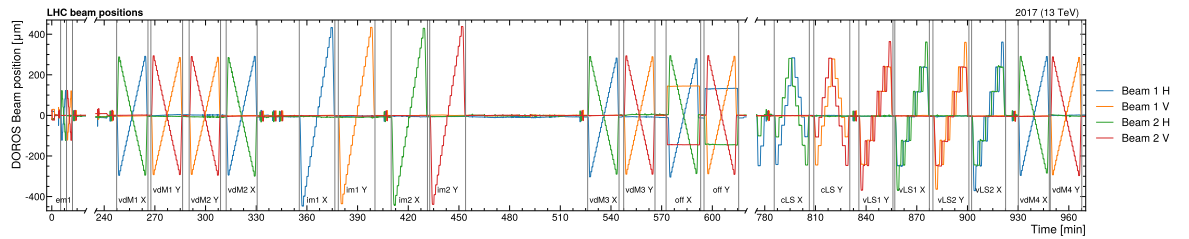


Fig. 3.5 Vertical (V) and horizontal (H) beam positions as a function of time measured by the DOROS beam position monitors during LHC fill 6016. The orbit is averaged over the bunches and monitored throughout the scan program with 1 second time granularity. The individual scans are delimited by the vertical lines. Each scan pair consists of two scans orthogonal to each other and labelled with the abbreviation of the specific scan type

529 3.4.2 2018 vdM scan program

530 The 2018 vdM scan program was conducted during LHC fill 6868 from June 30 to July 1,
 531 2018, at a center-of-mass energy of 13 TeV. The LHC filling scheme included 124 colliding
 532 bunch pairs at the CMS interaction point (IP5). For the special case of PCC, to ensure a
 533 dataset with a high event count at large beam separations, CMS gated the zero-bias triggers
 534 on 5 bunch pairs (BCIDs 265, 865, 1780, 2192, and 3380) and recorded events at a total
 535 rate of 27 kHz.

536 The bunch intensities were approximately $7 - 9 \times 10^{10}$ protons per filled bunch, result-
 537 ing in a total beam intensity of approximately 4.5×10^{13} protons per beam. The total beam
 538 intensities were measured with the DC Current Transformers (DCCT) [17]. The beam
 539 orbit was monitored using two systems: the DOROS beam position monitors (BPMs) [18],
 540 located near IP5, and the arc BPMs, located in the LHC arcs adjacent to CMS.

541 The vdM scan program was conducted in two parts due to an alarm and a power cut.
542 The first part consisted of a total of five x-y scan pairs. First, two short emittance scans,
543 em1 (1) and em2 (2), were conducted, respectively. Then, a standard vdM scan pair, vdM1
544 (3), was performed, followed by an offset scan, off1 (4). Finally, a pair of beam imaging
545 scans, BI1 (5) and BI2 (6), were conducted, but only the first was completed before the
546 alarm interrupted the program.

547 The second part of the program was conducted approximately 7.5 hours later and
548 consisted of 12 scan pairs. Scan pair em3 (6) was a short emittance scan, followed by
549 beam imaging scan pairs Im3 (7) and Im4 (8), then an offset scan pair, off2 (9), and finally
550 two standard vdM scan pairs, vdM2 (10) and vdM3 (11). The latter two allowed us to test
551 the reproducibility of the measurement.

552 A length scale calibration program was performed after vdM3 using constant-separation
553 and variable-separation scan pairs: cLS (12), vLS1 (13), and vLS2 (14). Finally, a standard
554 vdM scan pair, vdM4 (15), and two short emittance scan pairs, em4 (16) and em5 (17),
555 concluded the program.

556 In each scan pair, the scan was performed first in the x direction and then in the
557 y direction, with the exception of the variable vLS calibration scan pairs, which were
558 performed in the opposite order.

559 Additionally, two Super Separation periods were conducted. The first, SS1, took place
560 right after vdM3 was completed, and the second, SS2, followed vdM4. These periods are
561 not included in the final count of scan pairs since they only involve separating the beams
562 in a single direction. They are used for the final estimation of background noise, which
563 will be subtracted in the final analysis. The details of these periods will be discussed in the
564 following chapter.

565 The bottom of Figure 3.6 shows the beam positions for the two beams in the x and
566 y directions as measured by the DOROS BPMs during the 2018 scan program, showing
567 the 17 scan pairs: 4 regular scan pairs, the 3 beam imaging scan pairs, the 2 offset scan
568 pair, and the 3 length scales, the emittance scan and the 2 Superseparation periods with the
569 corresponding abbreviations used.

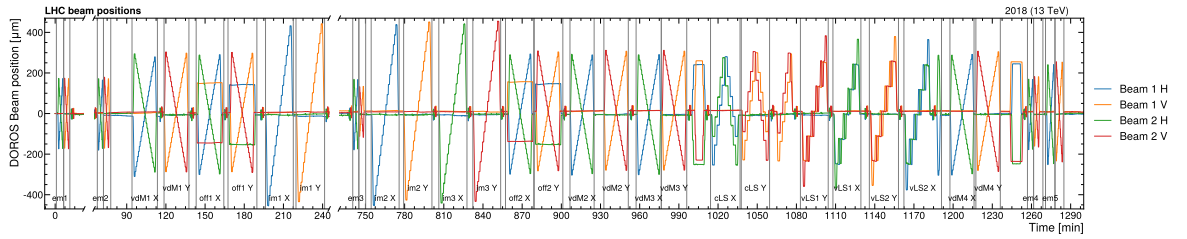


Fig. 3.6 Vertical (V) and horizontal (H) beam positions as a function of time measured by the DOROS beam position monitors during LHC fill 6868. The orbit is averaged over the bunches and monitored throughout the scan program with 1 second time granularity. The individual scans are delimited by the vertical lines. Each scan pair consists of two scans orthogonal to each other and labelled with the abbreviation of the specific scan type.

Chapter 4

Analysis and Results

The analysis of the luminosity calibration obtained with the PCC detector for the publication "Precision luminosity measurement at CMS in proton-proton collisions at 13 TeV in 2017 and 2018" was successfully conducted, yielding final results that will be included in the official publication of this study.

This chapter presents a detailed explanation of the entire analysis and processing workflow, from raw data acquisition, background analysis, and the selection of valid modules (veto modules), to the final calibration, which consists of the determination of the detector's visible cross-section σ_{vis} .

Finally, cross-checks were performed with other luminometers, along with final comparisons against the integrated luminosity of the entire year, to evaluate and determine the final uncertainties.

4.1 Data acquisition and processing

4.2 Module selection

To ensure accurate luminosity measurement, a module selection process is performed to exclude modules exhibiting instability or non-linearity across different data-taking periods, as these indicate non-physical shifts in cluster counts. Only stable pixel detector modules are used for PCC rate measurements, excluding defective modules or those significantly affected by readout buffer limitations [25].

The pixel system consists of 1856 modules, all initially considered for luminosity measurement. However, instabilities and non-linear effects can compromise accuracy. To identify "good" and "stable" modules, a selection is made by eliminating underperforming

modules based on their relative contribution to the cross section. Modules with consistent contributions across standard physics runs are retained, while those showing significant deviations from the average are excluded.

The pixel detector undergoes changes over time due to factors such as detector noise, aging, and radiation damage, leading to variations in the number of well-performing modules. These variations are assessed at a 23-second granularity, matching the luminosity database.

The procesos para module selection follows these steps:

- Low statistics lumisections are removed from the analisis for each period.
- The innermost layer (layer 0) of the pixel detector is excluded from the analysis due to significant dynamic inefficiency effects [11]. At higher \mathcal{L}_{inst} , the hit efficiency in this layer decreases because the readout chip cannot process all of the hits.
- A loose selection of 7% based on RMS/mean from the module weight distribution (changes in the module PCC ratio relative to the total PCC) is applied. Modules with significantly large RMS/mean are removed with this selection as shown in 4.1.
- The module stability is re-evaluated based on RMS/mean values using an iterative method where the second iteration is made with a loose selection of 2%.

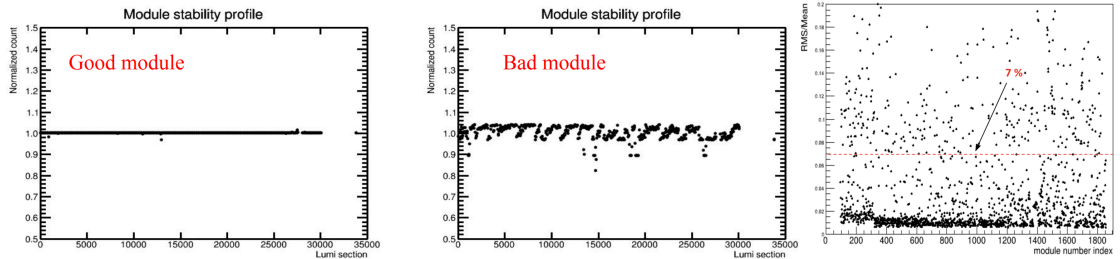


Fig. 4.1 left: stability profile for good and bad modules where weight is plotted as a function of lumi section. Right: RMS/mean values of module weight for all pixel modules where each pixel module is represented by a module number index (same happen for the 4% iteration).

To ensure accuracy, pixel module veto lists were generated for different time periods using the procedure described above. To further improve stability, a common module veto list was created by merging the lists from all periods. Modules consistently identified as "bad" across multiple periods were excluded. The PCC data with zero bias was then reprocessed using this common veto list for the final vdM analysis.

4.2.1 2017 Pixel Detector module selection

The 2017 PCC data is divided into five periods (datasets) throughout the year: B, C, D, E, and F. The selection of stable ("good") detector modules is based on analyzing each module's cluster count relative to the total (module weight), as described earlier in this section. The module weight is computed for each data period and compared across periods to assess stability.

During the final part of the 2017 run, power supply failures led to a significant number of non-operational modules, which were excluded from the final measurement. In particular, the Pixel detector experienced issues with DC-DC power converters during period F, resulting in a large number of unstable modules. Therefore, the stability analysis begins by comparing module weights between periods D and F.

Variations in module weight across periods are used to identify unstable modules. Table 4.1 presents the selection criteria applied in each comparison and the number of modules that meet these criteria.

Table 4.1 PCC 2017 detector module stability selections applied to the module weights

Periods	# Good modules
D + F	945
D + B	945
D + C	945
D + E	859
B + F	819
B + C	807
B + E	810
E + C	901
E + F	756
C + F	907
Combined	633

The number of selected modules for the final analysis was **633 (34.1%) for 2017**.

4.2.2 2018 Pixel Detector module selection

The recorded data from 2018 is divided into seven periods: A, B, C, D1, D2, D3, and D4. The vdM calibration data (LHC Fill 6868) is part of period B. The module vetolist is first created for period B and the vdM fill, and then extended to the other periods (A, C, D1, D2, D3, and D4).

To determine the list of good modules, the ZeroBias data is processed by analyzing the cluster count of each module relative to the total count (module weight), following the method described at the beginning of this section. A bootstrap procedure is then applied to remove unstable modules.

As explained earlier, as a first steps, for each period, lumisections with poor PCC statistics are removed by applying a selection based on total PCC and all barrel layer 1 modules are excluded due to their significant sensitivity to dynamic inefficiency effects. The following describes the procedure applied to different periods.

For period B and the vdM fill, an initial 7% selection is applied to remove unstable modules. The stability of the remaining modules is then re-evaluated based on updated module weights, and a final 2% selection is applied using the recalculated RMS/Mean values.

In periods A, C, and D, the module selection from period B serves as the starting point. The same procedure is applied, including the two-step selection with 7% and 2% thresholds. Additionally, module weight variations between period B and these periods are examined, and modules with a deviation greater than three sigma from the mean are removed.

A common module list was created by combining all exclusive module lists from different period combinations. Table 4.2 presents the number of good modules after sequentially combining each period.

Table 4.2 Common module vetolist created by combining module vetolists for each period using a 2% quality selection as described in the text.

Period	# bad modules	# good modules
B	802	1054
B + C	1076	780
A + B + C	1417	439
A + B + C + D1	1534	322
A + B + C + D1 + D2	1629	227
A + B + C + D1 + D2 + D3	1668	188
A + B + C + D1 + D2 + D3 + D4	1701	155

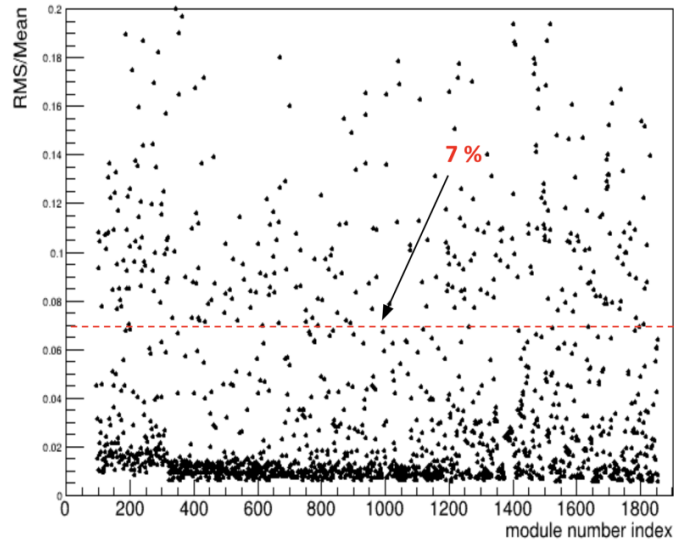


Fig. 4.2 rms/mean of module weight profile for all modules. A loose selection of 7% is applied to remove bad modules. Appropriate selections are applied in each iterative step to remove other bad modules.

652 The number of selected modules for the final analysis was **155 (8.35%) in 2018**.

653 The relative contribution of each pixel detector layer and disk to the total PCC, after
 654 applying the final module selection, is shown in Fig. 4.3 as a function of time throughout the year.

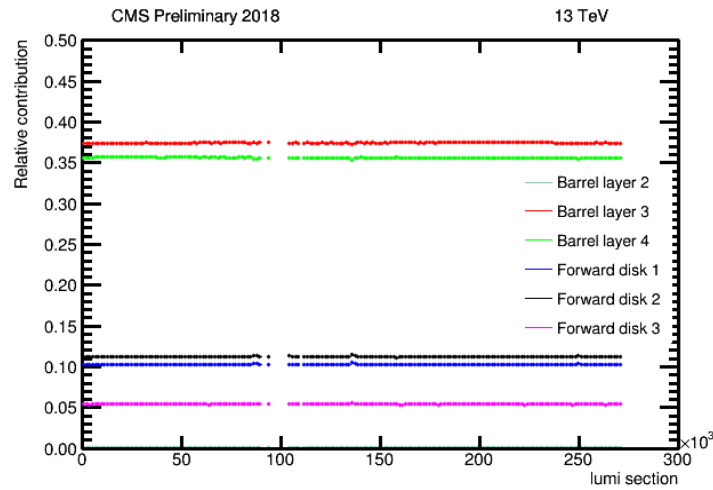


Fig. 4.3 Stability profiles of Pixel detector layers and disks with the final module selection.

655

4.3 Background estimation

To perform accurate fitting of the data, it is necessary to take into account the following background contributions to the PCC rates. These contributions are estimated independently during the Super Separation (SS) periods discussed in the previous section. Three primary sources of beam-induced background should be considered:

- **Beam Halo (BH):** This component occurs when the secondary particles reach the experimental cavern from the LHC tunnel. The primary beam halo is the population of beam protons characterized by offsets in the transverse coordinates, travelling in radial amplitude around the beam axis and being captured mostly by the LHC collimation system. In every step of the multi-stage cleaning system of the LHC, more halo particles are captured but also secondary showers are created by the interaction of the beam particles with the collimator material. The largest contribution of the beam halo to the background consist of secondary particles that stem from the interactions of the beam halo particles at the tertiary collimators and arrive in large radius into the CMS cavern [19].
- **Beam Gas Inelastic (BGI):** This component arises from all inelastic interactions between primary beam protons and residual gas in the beam pipe. The interaction rate is largely influenced by the quality of the vacuum in the various beam line elements upstream of CMS, so the source of this contribution is distributed throughout the long straight section [20].
- **Beam Gas Elastic (BGE):** The elastic beam gas contribution is made up of all the coherent and quasi-elastic, nuclear elastic, and Coulomb scattering for multi-turn beam-gas interactions around the ring. [20].

4.3.1 Background estimation for 2017 data

4.3.2 Background estimation for 2018 data

4.4 Beam Corrections

4.5 Fit Model Selection

After testing several mathematical fit models, the chosen model with the best fit quality and after applying all the corrections mentioned earlier, was a double Gaussian function:

$$Poly4G(x) = A \left[1 + a_2 \left(\frac{-(x - \bar{x})}{\sigma} \right)^2 + a_4 \left(\frac{-(x - \bar{x})}{\sigma} \right)^4 \right] \exp \left[-\frac{(x - \bar{x})^2}{2\sigma^2} \right] \quad (4.1)$$

$$Poly4G(x) = A \left(1 + a_2 \left(\frac{-(x - \bar{x})}{\sigma} \right)^2 + a_4 \left(\frac{-(x - \bar{x})}{\sigma} \right)^4 \right) \exp \left(-\frac{(x - \bar{x})^2}{2\sigma^2} \right) \quad (4.2)$$

- 685 • P the *peak* rate.
- 686 • F is the fraction of the peak rate attributed to the first Gaussian in the sum.
- 687 • x is the beam position.
- 688 • \bar{x} is the mean.
- 689 • Σ is the overlap between the beams.
- 690 • R is the ratio between the standard deviations of the Gaussians (first over the second).

691 4.6 Visible cross section results

692 4.7 Cross-detector comparisons

693 4.8 Systematic Uncertainties

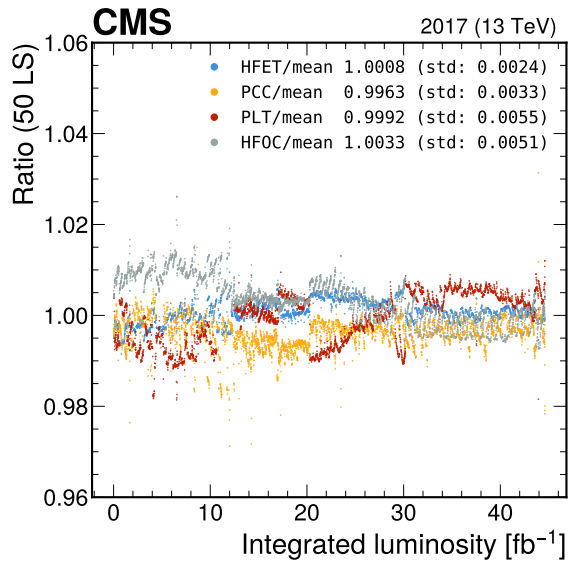


Fig. 4.4 Beam Position at the vdM Scan Program 2017 [9].

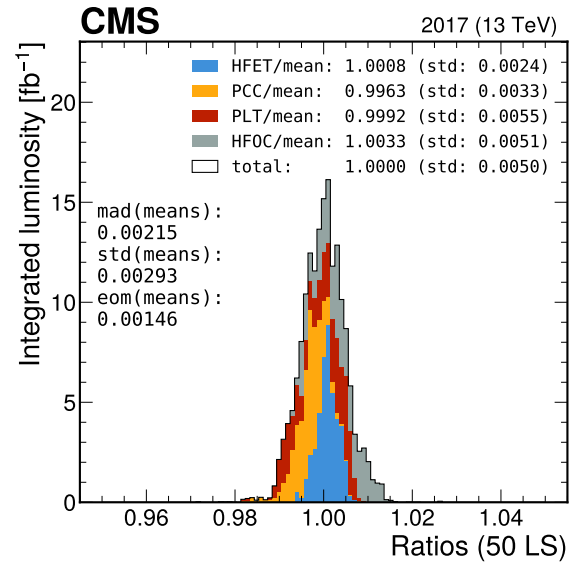


Fig. 4.5 Another image caption.

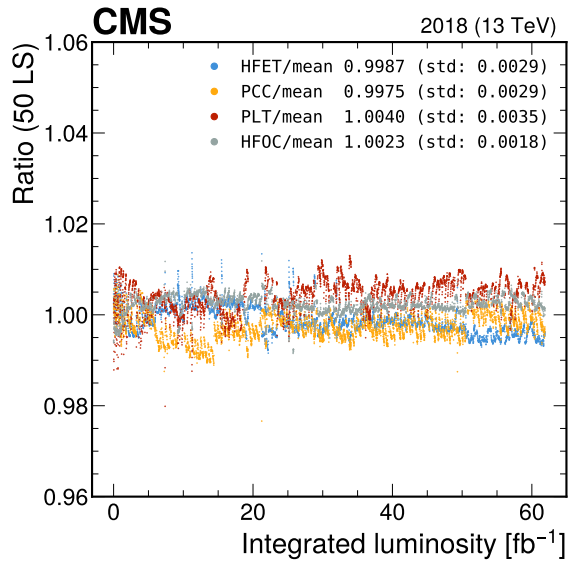


Fig. 4.6 Beam Position at the vdM Scan Program 2017 [9].

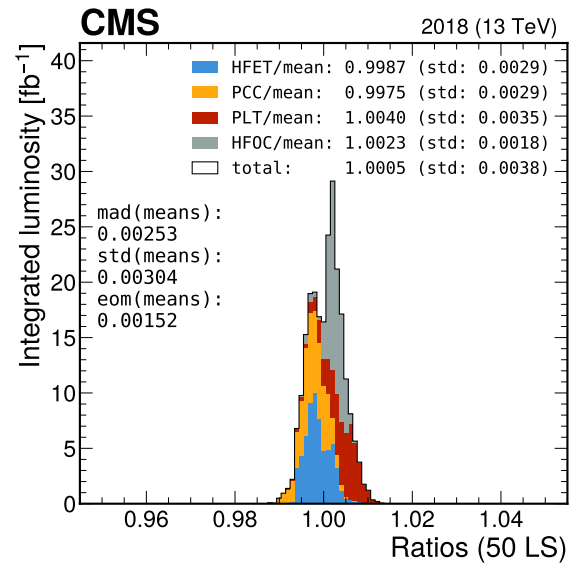


Fig. 4.7 Another image caption.

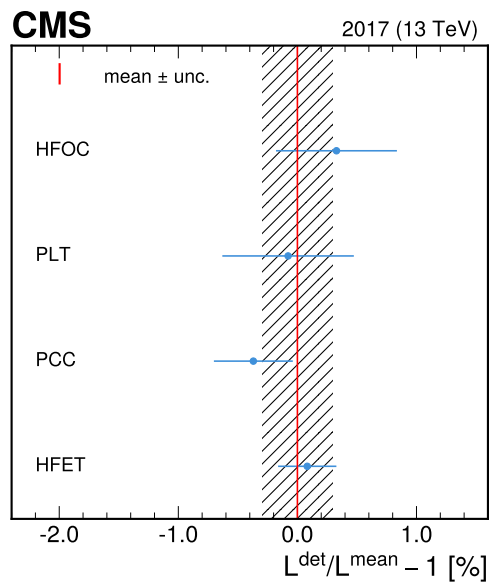


Fig. 4.8 Beam Position at the vdM Scan Program 2017 [9].

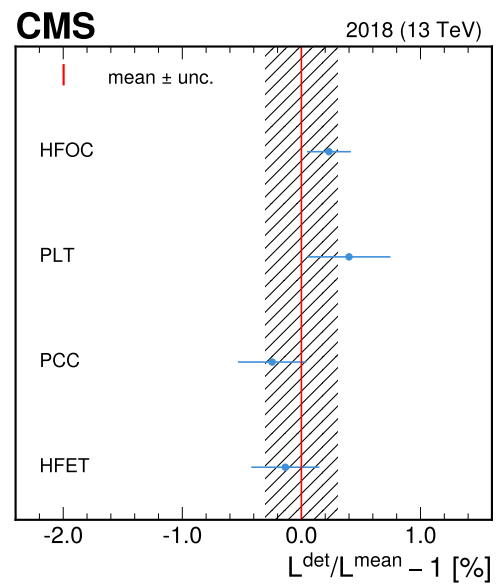


Fig. 4.9 Another image caption.

694 **Chapter 5**

695 **Summary and Outlook**

References

- 697 [1] M. Thomson, *Modern Particle Physics*, Cambridge University Press, New York,
698 2013.
- 699 [2] D. Griffiths, *Introduction to Elementary Particles; Second edition*, WILEY-VCH
700 Verlag GmbH Co. KGaA. Weinheim, Federal Republic of Germany, 2008.
- 701 [3] A. Belyaev and R. Douglas, *The Basics of Nuclear and Particle Physics*,
702 Springer (Undergraduate Texts in Physics Series), Switzerland, 2021, doi:
703 <https://doi.org/10.1007/978-3-030-80116-8>.
- 704 [4] S. Myers and H. Schopper, *Particle Physics Reference Library, volume 3*, Springer,
705 2020, doi: <https://doi.org/10.1007/978-3-030-34245-6>.
- 706 [5] W. Herr and B. Muratori, "Concept of Luminosity", CERN Document Server, 2016,
707 doi : 10.5170/CERN-2006-002.361.
- 708 [6] P. Traczyk, Online article : "Why precision luminosity measurements matter", 2022,
709 URL [https://home.cern/news/news/physics/why-precision-luminosity-measurements-](https://home.cern/news/news/physics/why-precision-luminosity-measurements-matter)
710 [matter](https://home.cern/news/news/physics/why-precision-luminosity-measurements-matter).
- 711 [7] CMS Collaboration, "Measurement of inclusive W and Z boson production cross
712 sections in pp collisions at $\sqrt{s} = 13$ TeV", CMS Physics Analysis Summary CMS-
713 PAS-SMP-15-004, 2015.
- 714 [8] Online article: "The Large Hadron Collider", 2023, URL [https://home.cern/science](https://home.cern/science/accelerators/large-hadron-collider)
715 [/accelerators/large-hadron-collider](https://home.cern/science/accelerators/large-hadron-collider).
- 716 [9] E. Halkiadakis and U. Rutgers, "Introduction to the LHC Experiments", May 2010,
717 doi: 10.1142/9789814327183_0009, arXiv: 1004.5564.
- 718 [10] CMS Collaboration, "CMS luminosity measurement for the 2017 data-taking period
719 at $\sqrt{s} = 13$ TeV", CMS Physics Analysis Summary CMS-PAS-LUM-17-004, 2018.
- 720 [11] CMS Collaboration, "CMS luminosity measurement for the 2018 data-taking period
721 at $\sqrt{s} = 13$ TeV", CMS Physics Analysis Summary CMS-PAS-LUM-18-002, 2019.
- 722 [12] CMS Collaboration, "CMS Luminosity Based on Pixel Cluster Counting - Summer
723 2012 Update", CMS Physics Analysis Summary CMS-PAS-LUM-12-001, 2012.
- 724 [13] CMS Collaboration, "Precision luminosity measurement in proton-proton collisions
725 at $\sqrt{s} = 13$ TeV in 2015 and 2016 at CMS, *Eur. Phys. J. C* **81** 800, 2021, doi:
726 [10.1140/epjc/s10052-021-09538-2](https://doi.org/10.1140/epjc/s10052-021-09538-2), arXiv: 2104.01927.

- 727 [14] Online resource: "CMS Luminosity - Public Results", 2023, URL
728 <https://twiki.cern.ch/twiki/bin/view/CMSPublic/LumiPublicResults> .
- 729 [15] CMS Collaboration, "The Phase-2 Upgrade of the CMS Beam Radiation, Instru-
730 mentation, and Luminosity Detectors: Conceptual Design", CMS-NOTE-2019-008,
731 2020.
- 732 [16] O. Karacheban, "Performance of the BRIL luminometers at CMS in Run 2", CMS
733 Public Note CMS-CR-2019-140, 2019, doi: 10.22323/1.364.0194.
- 734 [17] C. Barschel et al., "Results of the LHC DCCT calibration studies", Technical Report
735 2349 CERN-ATS-Note-2012-026 PERF, 2012.
- 736 [18] M. Gasior, J. Olexa, and R. Steinhagen, "BPM electronics based on compensated
737 diode detectors — results from development systems", Conf. Proc. C1204151 (2012).
- 738 [19] S. Orfanelli et al, "A novel Beam Halo Monitor for the CMS experiment at the LHC",
739 *JINST* **10** P11011, 2015, doi: 10.1088/1748-0221/10/11/P11011.
- 740 [20] S. Müller, "Simulation of beam-induced backgrounds in comparison with
741 data from the CMS pixel and other inner radii detectors", *Nuclear In-*
742 *struments and Methods in Physics Research Section A* **650** **1**, 2011, doi:
743 <https://doi.org/10.1016/j.nima.2010.11.082>.